

(TMD) [3, 9, 10] and three-dimensional topological materials [11–13], and has been experimentally observed, such as in Weyl semimetal WTe_2 [4] or TaIrTe_4 [14] and strained monolayer WSe_2 [15].

The nonvanishing nonlinear Hall effect in conventional materials attributes to a common trait: Strong spin-orbit coupling and the presence of low-energy Dirac quasiparticles forming titled Dirac cones. Recently, it was reported that sizable BCD can be caused by warping of the Fermi surface in strained graphene [16–18], in which the spin-orbit coupling and titled Dirac cones are completely absent. The nonzero BCD in strained graphene is ascribed to the higher order warping of Fermi surface and gives rise to nonlinear Hall effect. Recently, it was found that the nonlinear anomalous Nernst effect also appears in strained graphene as a result of trigonal warping of the Fermi surface [19]. Thus, monolayer graphene or TMD provides an exceptional platform to modulate and investigate the BCD through strain. In these time-reversal invariant two-dimensional strained materials, the nonlinear Hall effect usually stems from the BCD but not the QMD which needs breaking time-reversal symmetry [20].

Above scenario is suitable for the nonlinear response with respect to the charge degrees of freedom. Except for the charge, graphene or TMD usually has valley degrees of freedom. Valleys are the degenerate energy extrema of the electronic bands in momentum space and become well-defined degrees of freedom when they are well separated in momentum space with negligible inter-valley scattering. The valley degree of freedom has attracted significant attention, giving birth to the field of valleytronics [21–23]. Intriguingly, very recently, Das *et al.* [24] proposed a nonlinear valley Hall effect, which can be induced by QMD even in time-reversal symmetry, in spite of vanishing nonlinear charge Hall effect. As extending nonlinear response from charge degrees of freedom to valley, on one hand, the requirement for symmetry changes, and on the other hand, there arises a fundamental question: Whether we can give common interpretation about the nonlinear charge and nonlinear valley Hall effect. In linear valley Hall effect [25] and nonlinear valley Hall effect [24], both are ascribed to orbital magnetic moment (OMM) [26, 27]. We expect the nonlinear charge Hall effect also can be interpreted with OMM. Thus, we can understand the microscopic origin of both the nonlinear charge and nonlinear valley Hall effect in terms of the OMM [28–31].

In this work, we give a common interpretation about the nonlinear charge and nonlinear valley Hall effect. We reveal that both the charge/valley nonlinear responses with respect to the quadratical electric field \mathbf{E}^2 can be understood with a two-step process: The first step is generation of a nonequilibrium OMM by one electric field \mathbf{E} and then under the OMM the Hall effect is formed by another electric field \mathbf{E} . While the previous

works attributed the nonlinear Hall effect under the time-reversal symmetry to the BCD mechanism, we provide deeper insights with respect to the nonequilibrium OMM. Thus, we bridge between seemingly different effects — nonlinear charge and nonlinear valley hall effects, and unify them into a single physical picture based on different types of nonequilibrium OMM. Specifically, we find that the nonequilibrium OMM induced by shift of Fermi surface is valley-independent, which leads to the BCD induced nonlinear charge Hall current [26, 32–36]. In contrast, the nonequilibrium orbital magnetization induced by electric field corrected Berry curvature or QMD is valley-contrasting, which leads to QMD-induced nonlinear valley Hall effect. Therefore, the nonlinear charge current and nonlinear valley current essentially have the same physics and the dependence of valley index of the OMM determines which nonlinear Hall effect emerges. We investigate them by employing the strained graphene under uniaxial deformation. Furthermore, it is found that the nonlinear charge/valley Hall current can be distinguished from each other since they appear along orthogonality direction. We also in detail discuss the influence of various parameters, such as strain, mass gap, and chemical potential.

2 Model and theory

We consider electrons hopping on a honeycomb lattice, whose dynamics are governed by the nearest-neighbor tight-binding Hamiltonian

$$H = \sum_{\mathbf{R}, \delta} t(\mathbf{R}, \delta) c_A^\dagger(\mathbf{R}) c_B(\mathbf{R} + \delta) + H.C., \quad (1)$$

where \mathbf{R} denotes a position on the Bravais lattice and δ is the vector connecting this site to its nearest neighbors. The operators $c_A(\mathbf{R})$ and $c_B(\mathbf{R})$ correspond to the field operators on the A and B sublattices, respectively. We only need to consider three independent hopping parameters: $t_1 = t(\delta_1)$, $t_2 = t(\delta_2)$, and $t_3 = t(\delta_3)$. When one chooses x -axis along zigzag direction, the relative positions of the three nearest-neighbor B-sublattice atoms with respect to a given A-sublattice atom are given by $\delta_1 = (0, a/\sqrt{3})$, $\delta_2 = (a/2, -a/2\sqrt{3})$, and $\delta_3 = (-a/2, -a/2\sqrt{3})$. Here a denotes the lattice constant.

By transforming Eq. (1) into the momentum space, one can write the two-band Hamiltonian as $H = \sum_{\mathbf{q}} c^\dagger(\mathbf{q}) H(\mathbf{q}) c(\mathbf{q})$, where $c(\mathbf{q}) = [c_A(\mathbf{q}), c_B(\mathbf{q})]^T$ with

$$H(\mathbf{q}) = \begin{pmatrix} \frac{\Delta}{2} & -\sum_n t_n e^{i\mathbf{q} \cdot \delta_n} \\ -\sum_n t_n^* e^{-i\mathbf{q} \cdot \delta_n} & -\frac{\Delta}{2} \end{pmatrix}. \quad (2)$$

Here, Δ is a staggered potential between the two honey-



comb sublattices, which can be introduced by placing the graphene sheet on a substrate, for example, lattice-matched h-BN [37, 38]. This staggered chemical potential breaks inversion symmetry and allows for a nonvanishing Berry curvature.

In the absence of strain, due to the existence of a threefold rotation C_{3z} , after integration of the momentum, the BCD vanishes. When a specific strain is applied to the system, the nearest-neighbor hopping amplitudes are modulated by the strain [17, 39] as $t_n = t_0(1 - \beta \Delta u_n)$, where β is a material-dependent parameter, taking the value $\beta \simeq 2$ for graphene. The quantity Δu_n can be expressed in terms of the strain tensor ε_{ij} as $\Delta u_n = 3\delta_n^i \varepsilon_{ij} \delta_n^j / a^2$, where δ_n^i denotes the i -th component of the n -th nearest-neighbor vector. Throughout this work, we use the equilibrium carbon-carbon bond length $a = 1.42 \text{ \AA}$ as the unit of length.

By expanding Eq. (2) around the two inequivalent valleys $\mathbf{K}_{\pm} = (\pm 4\pi/3a \mp \frac{v_F A_x}{v_x}, 0)$, where we define the Fermi velocity as $v_F = \sqrt{3}t_0 a/2$, and the term including $A_x = \sqrt{3}\beta(\varepsilon_{xx} - \varepsilon_{yy})/2a$ is the shift of two valleys caused by the strain, we can obtain a low-energy effective Hamiltonian as [17]

$$H_{warped} = \xi v_x k_x \sigma_x + v_y k_y \sigma_y + (\lambda_1 k_y^2 - \lambda_2 k_x^2) \sigma_x + 2\xi \lambda_2 k_x k_y \sigma_y + \frac{\Delta}{2} \sigma_z. \quad (3)$$

Here, $\xi = \pm$ denotes the valley index, σ refers to the Pauli matrices acting on the sublattice degree of freedom. Under the strain, the velocities become anisotropic in the form of $v_x = v_F[1 - \beta(3\varepsilon_{xx} + \varepsilon_{yy})/4]$ and $v_y = v_F[1 - \beta(\varepsilon_{xx} + 3\varepsilon_{yy})/4]$. As retaining terms up to the second order in momentum, the band-warping effects are presented with the warping coefficients given by $\lambda_1 = \lambda_0[1 - \beta(5\varepsilon_{yy} - \varepsilon_{xx})/4]$ and $\lambda_2 = \lambda_0[1 - \beta(3\varepsilon_{xx} + \varepsilon_{yy})/4]$ with $\lambda_0 = t_0 a^2/8$. Anisotropic dispersion $v_x \neq v_y$ breaks the C_{3z} symmetry and the trigonal warping term breaks both the P and T symmetry for each valley.

By diagonalizing the Hamiltonian Eq. (3), we obtain the the energy dispersion as

$$\varepsilon_n(\mathbf{k}) = n \sqrt{d_x^2 + d_y^2 + d_z^2}, \quad (4)$$

where we denote $n = \pm$ for the conduction and valence bands, respectively, and $d_x = \lambda_1 k_y^2 - \lambda_2 k_x^2 + \xi v_x k_x$, $d_y = v_y k_y + 2\xi \lambda_2 k_x k_y$, and $d_z = \frac{\Delta}{2}$. The corresponding eigenstates are given by

$$\Psi_{\pm}(\mathbf{k}) = \frac{1}{\sqrt{2|\mathbf{d}_k|(\mathbf{d}_k \mp d_z)}} \begin{pmatrix} d_x - id_y \\ \pm |\mathbf{d}_k| - d_z \end{pmatrix}, \quad (5)$$

where $\mathbf{d}_k = (d_x, d_y, d_z)$.

In this work, we are interested in the second-order dc

nonlinear Hall conductivity. When applying an ac electric field $\mathbf{E}(\omega) = \Re(\mathbf{E}e^{i\omega t})$, the induced dc nonlinear current can be expressed as

$$j_a = -e \sum_{n,\mathbf{k}} \frac{d^2 \mathbf{k}}{(2\pi)^2} f_n(\mathbf{k}) v_a^n(\mathbf{k}), \quad (6)$$

where $f_n(\mathbf{k})$ and $v_a^n(\mathbf{k}) = (e/\hbar)\mathbf{E} \times \boldsymbol{\Omega}_n$ are distribution function and anomalous Hall velocity, respectively. Here, The Berry curvature is given by

$$\boldsymbol{\Omega}_n = 2eIm \sum_{m \neq n} \frac{[A_{nm}^a A_{mn}^b]}{\varepsilon_n - \varepsilon_m(\mathbf{k})}. \quad (7)$$

Usually, there are two mechanisms contributing to the nonlinear Hall current. One is the electric-field correction to distribution function $f_n(\mathbf{k}) \rightarrow e\tau E_b \partial_{k_b} f_0(\varepsilon_n)$, which is given by the Boltzmann equation under the relaxation time approximation. Here, τ denotes the scattering time and $f_0(\varepsilon_n) = 1/[1 + e^{(\varepsilon_n - \mu)/k_B T}]$ is the equilibrium Fermi-Dirac distribution with μ the chemical potential and T the temperature. When denoting $j_a = \chi_{a;bc} E_b E_c^*$ and performing the integration by parts, one can find the BCD nonlinear Hall conductivity as [3]

$$\chi_{a;bc}^{BCD} = -g_s \frac{e^3 \tau}{\hbar^2} \epsilon_{abd} \sum_{n,\mathbf{k}} (\partial_c \boldsymbol{\Omega}_n^d) f_0(\varepsilon_n), \quad (8)$$

where ϵ_{abc} is the Levi-Civita tensor, $g_s = 2$ accounts for spin degeneracy, and $a, b, c = (x, y, z)$ are Cartesian indices, respectively describing the current direction (a) and electric field direction (b, c).

The other is electric-field correction to the Berry curvature in the anomalous Hall velocity from interband coherence, namely, $v_a^n(\mathbf{k}) = (e/\hbar)\mathbf{E} \times \boldsymbol{\Omega}_n^E$, where the Berry curvature $\boldsymbol{\Omega}_n^E = \nabla_{\mathbf{k}} \times \mathbf{A}_n^E$ is corrected by an electric-field-corrected Berry connection [5, 35, 40, 41] $\mathbf{A}_{n;a}^E = G_n^{ab} E_b$. Here,

$$G_n^{ab} = e \sum_{m \neq n} \frac{Re[A_{nm}^a A_{mn}^b]}{\varepsilon_n - \varepsilon_m}, \quad (9)$$

is called the QMD or the Berry connection polarizability (BCP) tensor. Submitting Eq. (9) to Eq. (6) and keeping the electric field up to \mathbf{E}^2 term, one can obtain the corresponding intrinsic nonlinear Hall conductivity, given by [40]

$$\chi_{a;bc}^{BCP} = -g_s \frac{e^2}{2\hbar} \sum_{n,\mathbf{k}} (2\partial_a G_n^{bc} - \partial_b G_n^{ac} - \partial_c G_n^{ab}) f_0(\varepsilon_n). \quad (10)$$

In these nonlinear Hall effect, it is expected that the orbital magnetization will play a role. In the semiclassical picture, a Bloch electron is modeled by a wave packet in a Bloch band, which is found to rotate about its center

of mass in general, yielding an orbital magnetic moment given by

$$\mathbf{m}_n(\mathbf{k}) = -i \frac{e}{2\hbar} \langle \nabla_{\mathbf{k}} \Psi_n(\mathbf{k}) | \times [H(\mathbf{k}) - \varepsilon_n(\mathbf{k})] | \nabla_{\mathbf{k}} \Psi_n(\mathbf{k}) \rangle. \quad (11)$$

In the presence of a weak magnetic field B , the electron energy band is corrected to be $\varepsilon_n(\mathbf{k}) \rightarrow \varepsilon_n(\mathbf{k}) - \mathbf{m}_n(\mathbf{k}) \cdot \mathbf{B}$. For an equilibrium ensemble of electrons, taking the differential of the total energy with respect to \mathbf{B} , we can obtain the orbital magnetization at zero magnetic field to be [42]

$$\mathbf{M} = 2 \sum_{n,\mathbf{k}} f(\varepsilon_n) \left[\mathbf{m}_n(\mathbf{k}) + \frac{e\mathbf{\Omega}_n(\mathbf{k})}{\hbar} (\mu - \varepsilon_n(\mathbf{k})) \right]. \quad (12)$$

For a two-dimensional system under consideration, the OMM is always perpendicular to the material plane and only the out-of-plane orbital magnetization M_z survives.

3 Results and discussion

3.1 Equilibrium OMM induced linear valley Hall effect

Before performing the calculation of nonlinear transports, we firstly discuss the relation between the linear Hall effect and the equilibrium orbit magnetization $M_{eq}(\mathbf{k})$. The equilibrium OMM $M_{eq}(\mathbf{k})$ can be obtained from Eq. (12) with $f(\mathbf{k}) = f_0(\mathbf{k})$ chosen as the Fermi–Dirac distribution function, and so the OMM $M_{eq}(\mathbf{k})$ is independent of electric field \mathbf{E} . In Fig. 1(a) we present the distribution of the OMM $M_{eq}(\mathbf{k})$ along k_x direction for conduction band ($n = +$) and K valley ($\xi = +$). It is evident that $M_{eq}(\mathbf{k})$ always emerges, regardless of the existence of strain. Importantly, $M_{eq}(\mathbf{k})$ is mainly concentrated around the valley regions and takes opposite sign in two valleys. We can integrate $M_{eq}(\mathbf{k})$ over \mathbf{k} around each valley to obtain the valley orbital magnetization $M_{eq}(\xi)$, and plot it as a function of chemical potential μ in Fig. 1(b). Interestingly, $M_{eq}(\xi)$ has the same magnitude but with opposite sign at two valleys \mathbf{K} and \mathbf{K}' . Thus, the carriers from different valleys suffer from the opposite magnetization $M_{eq}(\mathbf{K}) = -M_{eq}(\mathbf{K}')$ and move towards opposite edge of the sample. It is just this valley-contrasting orbital magnetization that leads to the well-known valley Hall effect [25].

In Fig. 1(c), we plot the valley-resolved linear Hall conductivity χ_{yx}^ξ , defined by $j_y^\xi = \chi_{yx}^\xi E_x$, as a function of chemical potential μ . It is evident that due to χ_{yx}^ξ from each valley remaining finite and opposite sign, as indicated by the red and blue curves, the complete cancellation makes the charge Hall conductivity $\chi_{yx}^c = \chi_{yx}^K + \chi_{yx}^{K'}$ vanishes. Instead, this valley-contrasting response results in a finite valley Hall conductivity $\chi_{yx}^v = \chi_{yx}^K - \chi_{yx}^{K'}$. This

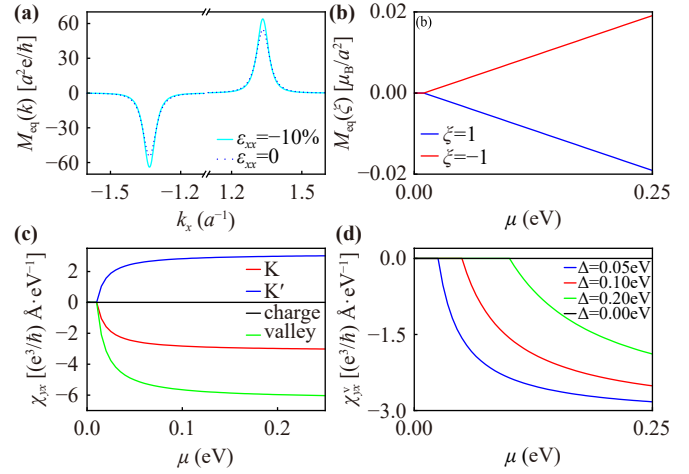


Fig. 1 (a) The distribution of the OMM $M_{eq}(\mathbf{k})$ along k_x direction with $k_y = 0$, for conduction band ($n = +$) and K valley ($\xi = +$), in the absence of and presence of strain $\varepsilon_{xx} = -10\%$ along the zigzag direction (i.e., x -axis). (b) Dependence on the chemical potential μ of the valley orbital magnetization $M_{eq}(\xi)$. (c) The valley-resolved linear Hall conductivity χ_{yx}^ξ as function of chemical potential μ . Due to χ_{yx}^ξ from each valley remaining finite and opposite sign, only the valley Hall conductivity χ_{yx}^v emerges while charge Hall conductivity χ_{yx}^c vanishes. (d) The variation of valley Hall conductivity χ_{yx}^v with the staggered potential Δ . We chose $\lambda_0 = 0.35$ eV, and here and thereafter, we use the equilibrium carbon–carbon bond length $a = 1.42$ Å as the unit of length.

is a result of time-reversal invariant. In Fig. 1(d), we depict the dependence of the valley Hall conductivity χ_{yx}^v on the staggered potential Δ . Obviously, χ_{yx}^v has wider zero-conductivity plateau with the increase of energy gap induced by Δ and vanishes in the presence of inversion symmetry, i.e., $\Delta = 0$.

3.2 Nonequilibrium shift OMM induced nonlinear charge Hall effect

Above, we discuss the relation of the valley orbital magnetization with linear valley Hall effect. It is interesting to extend this scenario to the nonlinear situation. When considering the OMM corrected up to the first order in the electric field, we have two choices: the correction of distribution function or the correction of $\mathbf{m}(\mathbf{k})$ and $\mathbf{\Omega}(\mathbf{k})$. Firstly, we discuss the first case. For the orbital magnetization in Eq. (12), according to Boltzmann equation we can correct the distribution function $f(\mathbf{k})$ up to the first-order in the electric field, which is approximated as $f(\mathbf{k}) \approx f_0[\varepsilon(\mathbf{k})] + (e/\hbar)\tau \mathbf{E} \cdot \partial_{\mathbf{k}} f_0[\varepsilon(\mathbf{k})]$. Thus, from Eq. (12) the electric-field corrected magnetization can be expressed as

$$\mathbf{M}_{\text{shift}} = \frac{2e\tau}{\hbar} \int \frac{d^2\mathbf{k}}{(2\pi)^2} \mathbf{E} \cdot \partial_{\mathbf{k}} f_0[\varepsilon(\mathbf{k})] \mathbf{m}(\mathbf{k}). \quad (13)$$

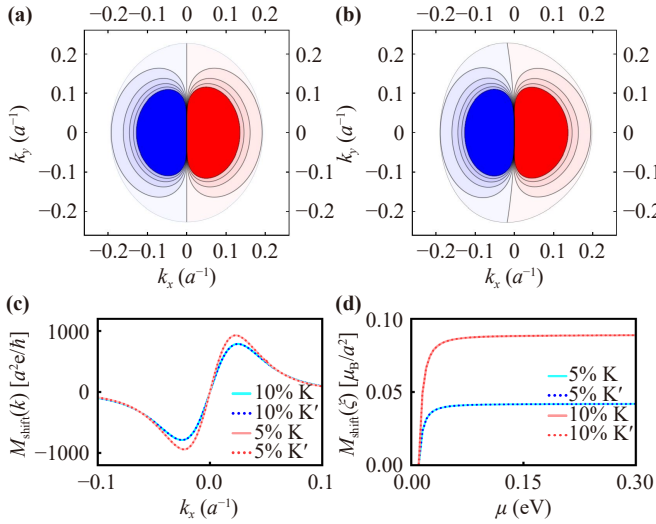


Fig. 2 The distribution of the OMM $M_{\text{shift}}(\mathbf{k})$ in the $(k_x - k_y)$ plane (a) in the absence of and (b) in the presence of the warping effect λ_0 . (c) The distribution of the OMM $M_{\text{shift}}(\mathbf{k})$ along k_x direction with $k_y = 0$. (d) Dependence on the chemical potential μ of the valley orbital magnetization $M_{\text{shift}}(\xi)$. In (c) and (d), different strain strength are plotted. The other parameters are chosen as $\Delta = 0.02$ eV, $\lambda_0 = 0.35$ eV, $\varepsilon_{xx} = 5\%$, and $\mu = 0.3$ eV.

At low temperatures, we use $\partial_{\mathbf{k}} f_0[\varepsilon(\mathbf{k})] = \frac{\partial \varepsilon(\mathbf{k})}{\partial \mathbf{k}} \delta(\varepsilon(\mathbf{k}) - \mu)$ to take a calculation. This correction originates from the shift of Fermi surface by the applied in-plane electric field, attributing to intraband contribution. Also, \mathbf{E} -corrected M_{shift} has only the out-of-plane component.

In Fig. 2, we depict the distribution of the orbit magnet momentum $M_{\text{shift}}(\mathbf{k})$ in momentum space (k_x, k_y) . In the presence of trigonal warping effect but without strain [seeing Fig. 2(a)], both the Fermi surface and $M_{\text{shift}}(\mathbf{k})$ for the \mathbf{K} valley become trigonal-like, namely C_{3z} rotation symmetry. After integration of \mathbf{k} , the orbital magnetization $M_{\text{shift}} = 0$, which perfectly cancels all contributions. Meantime, in the absence of trigonal warping effect (i.e., $\lambda_0 = 0$), although the shapes of the energy band and $M_{\text{shift}}(\mathbf{k})$ for the \mathbf{K} valley are distorted by strain, they are the odd function of \mathbf{k} . Only when both the strain and warping effect coexist, the Fermi surface and $M_{\text{shift}}(\mathbf{k})$ are distorted to be asymmetric, as shown in Fig. 2(b) where a uniaxial strain ε_{xx} is applied along x -axis, namely, along the zigzag direction of the crystal. Thus, after integrating of \mathbf{k} , finite M_{shift} will appear. As \mathbf{E} -corrected OMM $M_{\text{shift}}(\mathbf{k})$ is also mainly concentrated around two valleys, as shown in Fig. 2(c), we still can integrate $M_{\text{shift}}(\mathbf{k})$ around each valley to obtain the \mathbf{E} -corrected valley orbital magnetization $M_{\text{shift}}(\xi)$, which is plotted in Fig. 2(d) as a function of chemical potential μ . Notice that $M_{\text{shift}}(\mathbf{k})$ takes the same sign at two valleys, distinguishing from the equilibrium OMM $M_{\text{eq}}(\mathbf{k})$ which has opposite sign. As a result, the valley orbital magnetization $M_{\text{shift}}(\mathbf{K}) = M_{\text{shift}}(\mathbf{K}')$ is

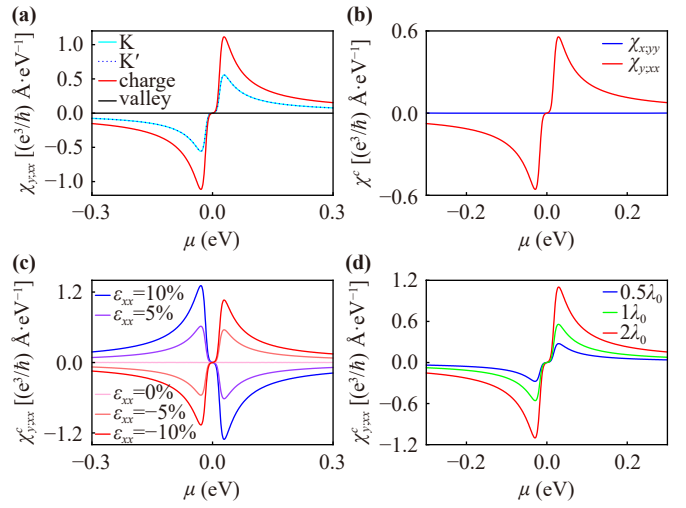


Fig. 3 (a) The valley-resolved nonlinear Hall conductivity $\chi_{y;xx}^{\xi}$ as a function of chemical potential μ , where only nonlinear charge Hall conductivity $\chi_{y;xx}^c$ exists and there is no nonlinear valley Hall conductivity $\chi_{y;xx}^v$. (b) The nonlinear charge Hall conductivity $\chi_{y;xx}^c$ and $\chi_{y;yy}^c$. Dependence of $\chi_{y;xx}^c$ on the strain strength ε_{xx} (c) and the warping parameter λ_0 (d). The other parameters are chosen as $\Delta = 0.03$ eV, $\lambda_0 = 0.35$ eV, $\hbar/\tau = 0.1$ meV, and $\varepsilon_{xx} = 5\%$.

strictly guaranteed. Thus, the carriers from different valleys suffer from the same orbital magnetization and move towards the same edge of the sample. We can understand the valley dependence from the viewpoint of symmetry. When taking an operation of spatial inversion (P), two valleys exchange each other $\mathbf{K} \leftrightarrow \mathbf{K}'$, and $\mathbf{k} \rightarrow -\mathbf{k}$ where \mathbf{k} is measured from the valley. It is easy to check that both $\mathbf{m}(\mathbf{k})$ and $\partial_{\mathbf{k}} f_0[\varepsilon(\mathbf{k})]$ is P-odd. Thus, their product is P-even, and after integrating over \mathbf{k} , the distribution-function-induced shift magnetization in Eq. (13) is valley-independent, producing a nonlinear charge Hall response. Figures 2(c) and (d) also show that the valley orbital magnetization increases with the enhancement of strain.

We calculate the BCD nonlinear Hall conductivity with Eq. (8), and in Fig. 3(a) the valley-resolved nonlinear Hall conductivity $\chi_{y;xx}^{\xi}$ is plotted as a function of chemical potential μ . It is evident that $\chi_{y;xx}^{\xi}$ from each valley has the same size and the same sign. Thus, there is no nonlinear valley Hall current $\chi_{a;bc}^v = \chi_{a;bc}^{\mathbf{K}} - \chi_{a;bc}^{\mathbf{K}'}$, but exists a nonlinear charge Hall current, defined by $\chi_{a;bc}^c = \chi_{a;bc}^{\mathbf{K}} + \chi_{a;bc}^{\mathbf{K}'}$. Physically, due to the valley-independent $M_{\text{shift}}(\mathbf{k})$, the carriers from different valleys suffer from the same magnetization and move towards the same edge of the sample. In contrast to the valley-contrasting orbital magnetization in linear valley Hall effect shown in Fig. 1, here the valley-independent orbital magnetization interprets the formation of BCD nonlinear Hall effect. We are known that the BCD-induced nonlinear Hall effect has been extensively received attention, but the underlying physics remains

to be uncovered. To be specific, here the nonlinear Hall conductivity $\chi_{y;xx}^\xi$ exhibits a second-order response to the electric field, and we can attribute it to a two-step process: One electric field E_x induces an orbital magnetization $M_{\text{shift}}(\xi)$ and then the other electric field E_x generates the anomalous Hall effect in the presence of the orbital magnetization.

In addition, in Fig. 3, one can notice that $\chi_{y;xx}^\xi$ exhibits a non-monotonic behavior, antisymmetric with respect to μ , characterized by two peaks in either side of the Dirac point, followed by a suppression for μ deviating from the Dirac point, which is essentially determined by the BCD. When chemical potential μ gets close to the Dirac point, the fermi surface manifests itself as a circle and the trigonal warping is not apparent, resulting in an almost vanishing nonlinear anomalous effect. As increasing the value of $|\mu|$, on one hand, the Berry curvature will decrease and tend to weaken the signal of nonlinear Hall effect, and on the other hand, the fermi surface will start to deviate from circle and the trigonal warping effect gradually becomes more profound which tends to enhance the nonlinear Hall effect. As a consequence, the competition between this two mechanisms cause the non-monotonic behavior.

Figure 3(b) shows that nonlinear charge Hall conductivity has direction selectivity. As one applies an external electric field E_y along the armchair direction (i.e., y -direction), $\chi_{x;yy}^\xi$ and $\chi_{x;yy}^c$ vanish. It is obvious that the threefold rotation C_{3z} about k_z is broken by the strain but the mirror symmetry M_{ky} is still survived. As we know, the BCD vector, defined by $D_a = \int \frac{d\mathbf{k}}{(2\pi)^2} f_0(\mathbf{k}) \frac{\partial \Omega_z(\mathbf{k})}{\partial k_a}$, always aligns with the mirror-symmetry axis, i.e., along the zigzag (x direction). Thus, $\chi_{y;xx}^\xi$ is finite for the electric field along the zigzag direction whereas $\chi_{x;yy}^\xi$ vanishes for the electric field along the armchair direction (y direction). In Fig. 3(c), we show that the nonlinear charge Hall conductivity $\chi_{y;xx}^c$ increases with the enhancement of strain $|\varepsilon_{xx}|$ and vanishes for $\varepsilon_{xx} = 0$. The underlying physics lies that as the strain increases, the electronic dispersion becomes more anisotropic, which leads to a pronounced enhancement of the orbital magnetization. Interestingly, when changing the strain from tensile strain ($\varepsilon_{xx} > 0$) to compressive strain ($\varepsilon_{xx} < 0$), the nonlinear charge Hall conductivity $\chi_{y;xx}^c$ inverses the sign, which is attributed to the inversion of the orbital magnetization M_{shift} . The nonlinear charge Hall conductivity $\chi_{y;xx}^c$ also becomes significant with the enhancement of warping effect λ_0 , as shown in Fig. 3(d). In addition, for the gapless energy with $\Delta = 0$, the orbital magnetization strictly remains zero and so nonlinear charge Hall current is zero.

3.3 Nonequilibrium intrinsic OMM induced nonlinear valley Hall effect

Finally, we discuss another case (2): The orbital magneti-

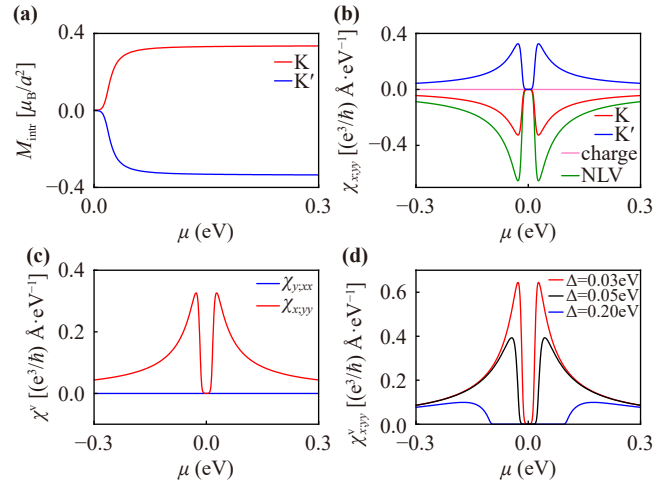


Fig. 4 (a) The valley-resolved intrinsic orbit magnetization M_{intr} and (b) the valley-resolved nonlinear Hall conductivity $\chi_{y;xx}^\xi$ as a function of chemical potential μ , here, only the nonlinear valley Hall conductivity $\chi_{x;yy}^v$ exists and there is no the nonlinear charge Hall conductivity $\chi_{x;yy}^c$. (c) The nonlinear valley Hall conductivity $\chi_{x;yy}^v$ and $\chi_{y;xx}^v$. (d) $\chi_{y;xx}^v$ as a function of μ for different staggered potential $\Delta = (0.03, 0.05, 0.20)$ eV. The other parameters are chosen as in Fig. 3.

zation in Eq. (12) corrected up to the first order in the electric field through $\mathbf{m}(\mathbf{k})$ and $\mathbf{\Omega}(\mathbf{k})$ has been derived in the semiclassical theory framework [24, 43, 44]. Due to the equilibrium distribution $f(\mathbf{k}) = f_0(\mathbf{k})$ remaining the Fermi-Dirac distribution function, the orbital magnetization derived from Eq. (12) is intrinsic, independent on impurity scattering. Under general two-band model, this intrinsic magnetization reduces to be

$$M_{\text{intr}} = \frac{e}{2} \sum_{n,m \neq n; \mathbf{k}} f_0(\mathbf{k}) \left[\frac{\partial \varepsilon_n(\mathbf{k})}{\partial k_b} G_n^{zd} + \frac{e}{\hbar} \varepsilon_{zbc} \frac{\partial \text{Re}[A_{nm}^c A_{mn}^d]}{\partial k_b} \right] E_d, \quad (14)$$

where the band-resolved quantum metric G_n^{zd} is defined in Eq. (9).

In Fig. 4(a), we depict the \mathbf{E} -corrected valley orbital magnetization $M_{\text{intr}}(\xi)$ as a function of chemical potential μ . Interestingly, this electric field-induced $M_{\text{intr}}(\xi)$ for each valley is also equal in magnitude but has the opposite sign, similar to the case of linear valley Hall effect in Fig. 1. Consequently, this valley-contrasting $M_{\text{intr}}(\mathbf{K}) = -M_{\text{intr}}(\mathbf{K}')$ forces the carriers from different valleys moving towards the opposite edge of the sample, causing the nonlinear valley Hall effect without the nonlinear charge Hall effect, as shown in Fig. 4(b). Here, the QMD nonlinear Hall conductivity is calculated with formula (10). Since the QMD in Eq. (14) is P-odd while the Fermi distribution $f_0[\varepsilon(\mathbf{k})]$ is P-even, their product is P-odd, leading to the valley-contrasting intrinsic magnetization in Eq. (14). Notice that the nonlinear valley Hall effect was reported in tilted massless Dirac fermions [24].

Despite of the different Hamiltonian, the underlying physics is the same for tilt and warping, both of which break the T and P symmetry for each valley but remain T and P symmetry globally. Once this symmetry is satisfied, the nonlinear valley Hall effect will appear. In these systems, the valley-contrasting orbital magnetization is essentially contributed by the BCP. Unlike the BCD nonlinear charge Hall effect, this second-order valley Hall effect does not always require gapped dispersion, as shown in Fig. 4(d) where Δ only changes the magnitude but is not decisive. As the nonlinear valley Hall effect $\chi_{y;xx}^v$ exhibits a non-monotonic behavior, it is symmetric with respect to μ .

In Fig. 4(c), it is noted that only $\chi_{x;yy}^v$ components of nonlinear valley Hall conductivity is finite while $\chi_{y;xx}^v$ vanishes, in contrast to the BCD induced nonlinear charge Hall effect. For the Hamiltonian Eq. (1), both nonlinear charge and valley Hall conductivities coexist but along orthogonal direction, which can be departed in experimental measurements. Due to the strain enhancing the breaking of symmetry, the nonlinear valley Hall conductivity $\chi_{x;yy}^v$ also becomes significant with the enhancement of strain, and changes the sign when the strain changes from $\varepsilon_{xx} > 0$ to $\varepsilon_{xx} < 0$.

4 Conclusion

In summary, we have presented a unified theoretical framework to understand the nonlinear valley Hall effect and nonlinear charge Hall effect in strained monolayer graphene. As we know, both of them can appear in the case of time-reversal symmetry, violating the theory of conventional linear Hall effect. Usually, the valley Hall effect is interpreted with OMM whereas nonlinear charge Hall effect is understood with BCD. In this work, we provide deeper insights into the nonlinear transports and find that both nonlinear valley and nonlinear charge Hall effects can be interpreted with the OMM. We employ an effective low-energy Hamiltonian of strained graphene, which is derived from a tight-binding model with strain-modified hopping parameters. Since strain induced anisotropic velocities and band-warping terms break the inversion and rotation symmetry, the nonlinear valley and charge Hall effect emerges. We demonstrate that the equilibrium OMM is valley-contrasting which contributes to the linear valley Hall current, the intrinsic OMM, originating from Berry curvature linearly corrected by electric field, is also valley-contrasting which contributes to the nonlinear valley Hall current, and the shift OMM, originating from Fermi distribution function linearly corrected by electric field, is valley-independent which contributes to the nonlinear BCD Hall current. Therefore, the nonlinear BCD Hall current and nonlinear valley current essentially have the same physics and the dependence of valley index of the OMM

determines which nonlinear Hall effect emerges. Meanwhile, the observed valley magnetization increases with the increasing magnitude of strain, reversibly turns on and off, and flips the sign, depending on the direction of strain, which provides a route to strain-engineered control of OMM and so the nonlinear transports. Notice that in our investigation, we employ the strained graphene only as an example to shed light on the unified framework for understanding both the nonlinear charge Hall and nonlinear valley Hall effects under the two-step mechanism. Naturally, this results are general and can be applied to the other noncentrosymmetric or ferrovalley two-dimensional materials where two-type nonlinear Hall effects coexist.

Experimentally, the orbital magnetization can be directly imaged via Magneto-optical Kerr effect (MOKE) microscopy as in Ref. [45]. The MOKE describes the rotation of polarization of linearly polarized light when reflected by a material in the presence of a magnetic field or magnetization, especially for out-of-plane magnetization in 2D materials. Here, both of the shift-induced and intrinsic orbital magnetization are out-of-plane and the MOKE microscopy is accessible. In addition, The shift-induced magnetization can be probed indirectly through standard second-harmonic transport experiments [4, 46] or orbital transfer torque exerted on the adjacent magnetizations as reported in recent works [47–50]. In contrast, the nonlinear valley Hall effect driven by intrinsic orbital magnetization cannot be directly measured due to no net charge current. But, one can excite electrons into a specific valley by illuminating with circularly polarized light, causing a finite anomalous Hall voltage whose sign is controlled by the helicity of the light as in Ref. [51].

Declarations The authors declare that they have no competing interests and there are no conflicts.

Acknowledgements This work was supported by the National Natural Science Foundation of China (Grant Nos. 12574050 and 12274146), the Guangdong Natural Science Foundation of China (Grant No. 2024A1515011300), Guangdong Basic and Applied Basic Research Foundation (Grant No. 2023B1515020050), and the Guangdong Provincial Quantum Science Strategic Initiative (Grant No. GDZX2401002).

References

1. C. Z. Chang, J. Zhang, X. Feng, J. Shen, Z. Zhang, M. Guo, K. Li, Y. Ou, P. Wei, L. L. Wang, Z. Q. Ji, Y. Feng, S. Ji, X. Chen, J. Jia, X. Dai, Z. Fang, S. C. Zhang, K. He, Y. Wang, L. Lu, X. C. Ma, and Q. K. Xue, Experimental observation of the quantum anomalous Hall effect in a magnetic topological insulator, *Science* 340(6129), 167 (2013)
2. H. Chen, Q. Niu, and A. H. MacDonald, Anomalous

- Hall effect arising from noncollinear antiferromagnetism, *Phys. Rev. Lett.* 112(1), 017205 (2014)
3. I. Sodemann and L. Fu, Quantum nonlinear Hall effect induced by berry curvature dipole in time-reversal invariant materials, *Phys. Rev. Lett.* 115(21), 216806 (2015)
 4. Q. Ma, S. Y. Xu, H. Shen, D. MacNeill, V. Fatemi, T. R. Chang, A. M. Mier Valdivia, S. Wu, Z. Du, C. H. Hsu, S. Fang, Q. D. Gibson, K. Watanabe, T. Taniguchi, R. J. Cava, E. Kaxiras, H. Z. Lu, H. Lin, L. Fu, N. Gedik, and P. Jarillo-Herrero, Observation of the nonlinear Hall effect under time-reversal-symmetric conditions, *Nature* 565(7739), 337 (2019)
 5. H. Liu, J. Zhao, Y. X. Huang, W. Wu, X. L. Sheng, C. Xiao, and S. A. Yang, Intrinsic second-order anomalous Hall effect and its application in compensated antiferromagnets, *Phys. Rev. Lett.* 127(27), 277202 (2021)
 6. S. Y. Xu, Electronic transport goes quantum at room temperature, *Nat. Phys.* 20(7), 1047 (2024)
 7. J. Wang, H. Zeng, W. Duan, and H. Huang, Intrinsic nonlinear Hall detection of the Néel vector for two-dimensional antiferromagnetic spintronics, *Phys. Rev. Lett.* 131(5), 056401 (2023)
 8. J. Y. Ba, Y. M. Wang, H. J. Duan, M. X. Deng, and R. Q. Wang, Nonlinear planar Hall effect induced by inter-band transitions: Application to surface states of topological insulators, *Phys. Rev. B* 108(24), L241104 (2023)
 9. J. S. You, S. Fang, S. -Y. Xu, E. Kaxiras, and T. Low, Berry curvature dipole current in the transition metal dichalcogenides family, *Phys. Rev. B* 98, 121109(R) (2018)
 10. Y. Zhang, Y. Sun, and B. Yan, Berry curvature dipole in Weyl semimetal materials: An *ab initio* study, *Phys. Rev. B* 97, 041101(R) (2018)
 11. J. I. Facio, D. Efremov, K. Koepf, J. S. You, I. Sodemann, and J. van den Brink, Strongly enhanced Berry dipole at topological phase transitions in BiTeI, *Phys. Rev. Lett.* 121(24), 246403 (2018)
 12. X. S. Li, C. Wang, M. X. Deng, H. J. Duan, P. H. Fu, R. Q. Wang, L. Sheng, and D. Y. Xing, Photon-induced Weyl half-metal phase and spin filter effect from topological Dirac semimetals, *Phys. Rev. Lett.* 123(20), 206601 (2019)
 13. C. Y. Zhu, S. H. Zheng, H. J. Duan, M. X. Deng, and R. Q. Wang, Double Andreev reflections at surface states of the topological insulators with hexagonal warping, *Front. Phys. (Beijing)* 15(2), 23602 (2020)
 14. A. Q. Wang, D. Li, T. Y. Zhao, X. Y. Liu, J. T. Zhang, X. Liao, Q. Yin, Z. C. Pan, P. Yu, and Z. M. Liao, Orbital anomalous Hall effect in the few-layer Weyl semimetal TaIrTe₄, *Phys. Rev. B* 110(15), 155434 (2024)
 15. M. S. Qin, P. F. Zhu, X. G. Ye, W. Z. Xu, Z. H. Song, J. Liang, K. Liu, and Z. M. Liao, Strain tunable berry curvature dipole, orbital magnetization and nonlinear Hall effect in WSe₂ monolayer, *Chin. Phys. Lett.* 38(1), 017301 (2021)
 16. K. Kang, T. Li, E. Sohn, J. Shan, and K. F. Mak, Nonlinear anomalous Hall effect in few-layer WTe₂, *Nat. Mater.* 18(4), 324 (2019)
 17. R. Battilomo, N. Scopigno, and C. Ortix, Berry curvature dipole in strained graphene: A Fermi surface warping effect, *Phys. Rev. Lett.* 123(19), 196403 (2019)
 18. X. G. Ye, Z. T. Zhang, P. F. Zhu, W. Z. Xu, A. Q. Wang, and Z. M. Liao, Engineering nonlinear Hall effect in bilayer graphene/black phosphorus heterostructures, *Phys. Rev. B* 111(4), L041403 (2025)
 19. Y. L. Wu, G. H. Zhu, and X. Q. Yu, Nonlinear anomalous Nernst effect in strained graphene induced by trigonal warping, *Phys. Rev. B* 104(19), 195427 (2021)
 20. T. Nag, S. K. Das, C. Zeng, and S. Nandy, Third-order Hall effect in the surface states of a topological insulator, *Phys. Rev. B* 107(24), 245141 (2023)
 21. Y. Wang, H. Sun, C. Wu, W. Zhang, S. D. Guo, Y. She, and P. Li, Multifield tunable valley splitting and anomalous valley Hall effect in two-dimensional antiferromagnetic MnBr, *Phys. Rev. B* 111(8), 085432 (2025)
 22. J. M. Lihm and C. H. Park, Nonlinear Hall effect from long-lived valley-polarizing relaxons, *Phys. Rev. Lett.* 132(10), 106402 (2024)
 23. J. R. Schaibley, H. Yu, G. Clark, P. Rivera, J. S. Ross, K. L. Seyler, W. Yao, and X. Xu, Valleytronics in 2D materials, *Nat. Rev. Mater.* 1(11), 16055 (2016)
 24. K. Das, K. Ghorai, D. Culcer, and A. Agarwal, Nonlinear valley Hall effect, *Phys. Rev. Lett.* 132(9), 096302 (2024)
 25. D. Xiao, W. Yao, and Q. Niu, Valley-contrasting physics in graphene: Magnetic moment and topological transport, *Phys. Rev. Lett.* 99(23), 236809 (2007)
 26. M. Koshino, Chiral orbital current and anomalous magnetic moment in gapped graphene, *Phys. Rev. B* 84(12), 125427 (2011)
 27. T. Thonhauser, D. Ceresoli, D. Vanderbilt, and R. Resta, Orbital magnetization in periodic insulators, *Phys. Rev. Lett.* 95(13), 137205 (2005)
 28. S. Pan, Z. Li, and Y. Han, Electric-field-tunable topological phases in valley-polarized quantum anomalous Hall systems with inequivalent exchange fields, *Front. Phys. (Beijing)* 20(1), 014207 (2025)
 29. S. Tamang, S. Verma, and T. Biswas, Orbital magnetization senses the topological phase transition in a spin-orbit coupled α -T₃ system, *Phys. Rev. B* 110(16), 165426 (2024)
 30. D. Li, X. Y. Liu, X. G. Ye, Z. C. Pan, W. Z. Xu, P. F. Zhu, A. Q. Wang, K. Watanabe, T. Taniguchi, and Z. M. Liao, Facilitating field-free perpendicular magnetization switching with a Berry curvature dipole in a Weyl semimetal, *Phys. Rev. B* 110(10), L100409 (2024)
 31. N. Kheirabadi, and A. Langari, Quantum nonlinear planar Hall effect in bilayer graphene: An orbital effect of a steady in-plane magnetic field, *Phys. Rev. B* 106(24), 245143 (2022)
 32. A. Huaman, and S. Barraza-Lopez, Winding Berry dipoles on uniaxially strained graphene/insulator moiré superlattices, *Phys. Rev. B* 111(4), L041103 (2025)
 33. C. Xiao, Z. Z. Du, and Q. Niu, Theory of nonlinear Hall effects: Modified semiclassics from quantum kinetics, *Phys. Rev. B* 100(16), 165422 (2019)
 34. J. Duan, Y. Jian, Y. Gao, H. Peng, J. Zhong, Q. Feng, J. Mao, and Y. Yao, Giant Second-Order Nonlinear Hall Effect in Twisted Bilayer Graphene, *Phys. Rev. Lett.* 129(18), 186801 (2022)



35. R. Chen, Z. Z. Du, H. P. Sun, H. Z. Lu, and X. C. Xie, Nonlinear Hall effect on a disordered lattice, *Phys. Rev. B* 110(8), L081301 (2024)
36. P. A. Pantalen, T. Low, and F. Guinea, *Phys. Rev. B* 103, 205403 (2021)
37. G. Giovannetti, P. A. Khomyakov, G. Brocks, P. J. Kelly, and J. van den Brink, Substrate-induced band gap in graphene on hexagonal boron nitride: *Ab initio* density functional calculations, *Phys. Rev. B Condens. Matter Mater. Phys.* 76(7), 073103 (2007)
38. C. L. Kane, and T. C. Lubensky, Topological boundary modes in isostatic lattices, *Nat. Phys.* 10(1), 39 (2014)
39. S. Y. Li, Y. Zhang, Y. N. Ren, J. Liu, X. Dai, and L. He, Experimental evidence for orbital magnetic moments generated by moiré-scale current loops in twisted bilayer graphene, *Phys. Rev. B* 102(12), 121406 (2020)
40. K. Das, S. Lahiri, R. B. Atencia, D. Culcer, and A. Agarwal, Intrinsic nonlinear conductivities induced by the quantum metric, *Phys. Rev. B* 108(20), L201405 (2023)
41. X. G. Ye, H. Liu, P. F. Zhu, W. Z. Xu, S. A. Yang, N. Shang, K. Liu, and Z. M. Liao, Control over Berry Curvature Dipole with Electric Field in WTe₂, *Phys. Rev. Lett.* 130(1), 016301 (2023)
42. D. Xiao, J. Shi, and Q. Niu, Berry Phase Correction to Electron Density of States in Solids, *Phys. Rev. Lett.* 95(13), 137204 (2005)
43. C. Xiao, H. Liu, J. Zhao, S. A. Yang, and Q. Niu, Thermoelectric generation of orbital magnetization in metals, *Phys. Rev. B* 103(4), 045401 (2021)
44. C. Xiao, Y. Ren, and B. Xiong, Adiabatically induced orbital magnetization, *Phys. Rev. B* 103(11), 115432 (2021)
45. J. Lee, K. F. Mak, and J. Shan, Electrical control of the valley Hall effect in bilayer MoS₂ transistors, *Nat. Nanotechnol.* 11(5), 421 (2016)
46. X. G. Ye, P. F. Zhu, W. Z. Xu, T. Y. Zhao, and Z. M. Liao, Nonlinear spin and orbital Edelstein effect in WTe₂, *Phys. Rev. B* 110(20), L201407 (2024)
47. X. G. Ye, P. F. Zhu, W. Z. Xu, N. Shang, K. Liu, and Z. M. Liao, Orbit-Transfer Torque Driven Field-Free Switching of Perpendicular Magnetization, *Chin. Phys. Lett.* 39(3), 037303 (2022)
48. Z. C. Pan, D. Li, X. G. Ye, Z. Chen, Z. H. Chen, A. Q. Wang, M. L. Tian, G. J. Yao, K. H. Liu, and Z. M. Liao, Room-temperature orbit-transfer torque enabling van der Waals magnetoresistive memories, *Sci. Bull. (Beijing)* 68(22), 2743 (2023)
49. R. Z. Niu, H. J. Duan, R. Ma, M. X. Deng, and R. Q. Wang, Current-induced time-reversal-even nonlinear spin polarization in p-wave magnets, *Phys. Rev. B* 113(4), 045101 (2026)
50. Y. L. Zhou, H. J. Duan, Y. J. Wu, M. X. Deng, L. Wang, D. Culcer, and R. Q. Wang, Nonlinear antidamping spin-orbit torque originating from intraband transport on the warped surface of a topological insulator, *Phys. Rev. B* 105(7), 075415 (2022)
51. K. F. Mak, K. L. McGill, J. Park, and P. L. McEuen, The valley Hall effect in MoS₂ transistors, *Science* 344(6191), 1489 (2014)